

Ab initio calculations of overlap integrals for $\mu \rightarrow e$ conversion in nuclei

Matthias Heinz,^{1,2,3,4,5} Martin Hoferichter,⁶ Takayuki Miyagi,^{7,1,2,3} Frederic Noël,⁶ and Achim Schwenk^{1,2,3}

¹*Technische Universität Darmstadt, Department of Physics, 64289 Darmstadt, Germany*

²*ExtreMe Matter Institute EMMI, GSI Helmholtzzentrum für Schwerionenforschung GmbH, 64291 Darmstadt, Germany*

³*Max-Planck-Institut für Kernphysik, Saupfercheckweg 1, 69117 Heidelberg, Germany*

⁴*National Center for Computational Sciences, Oak Ridge National Laboratory, Oak Ridge, TN 37831, USA*

⁵*Physics Division, Oak Ridge National Laboratory, Oak Ridge, TN 37831, USA*

⁶*Albert Einstein Center for Fundamental Physics, Institute for Theoretical Physics, University of Bern, Sidlerstrasse 5, 3012 Bern, Switzerland*

⁷*Center for Computational Sciences, University of Tsukuba, 1-1-1 Tennodai, Tsukuba 305-8577, Japan*

In an effective-field-theory approach, the rate for $\mu \rightarrow e$ conversion in nuclei depends on a set of effective operators mediating the lepton-flavor-violating interaction at a high scale, renormalization group corrections that describe the evolution to lower scales, and hadronic and nuclear matrix elements that turn quark-level interactions into hadronic ones and then embed the latter into nuclear responses. In particular, combining information from $\mu \rightarrow e\gamma$, $\mu \rightarrow 3e$, and $\mu \rightarrow e$ conversion in nuclei, it becomes possible to disentangle different underlying sources of lepton flavor violation. However, to assess the discriminatory power it is critical that uncertainties at each step of the analysis be controlled and fully quantified. In this regard, nuclear response functions related to the coupling to neutrons are notoriously problematic, since they are not directly constrained by experiment. We address these shortcomings by combining ab initio calculations with a recently improved determination of charge distributions from electron scattering by exploiting strong correlations among charge, point-proton, and point-neutron radii and densities. We present overlap integrals for ^{27}Al , ^{48}Ca , and ^{48}Ti including full covariance matrices, allowing, for the first time, for a comprehensive consideration of nuclear structure uncertainties in the interpretation of $\mu \rightarrow e$ experiments.

I. INTRODUCTION

Using effective-field-theory (EFT) methods, $\mu \rightarrow e$ conversion in nuclei can be described in a model-independent way in terms of lepton-flavor-violating (LFV) operators mediating the LFV interactions at a high scale while accounting for the different scales that play a role upon evolution to the low scale at which the experiment is performed [1–15]. To this end, first renormalization group corrections need to be considered to include the evolution to the lower scales [16–18], where then hadronic matrix elements turn the quark-level interactions into hadronic ones and nuclear matrix elements account for the strong-interaction effects of embedding the nucleons into the atomic nucleus. Finally, Coulomb corrections on the leptonic side of the interaction need to be considered, characterizing the influence of the potential generated by the nucleus on the initial bound-state muon and the ejected electron. Using such a framework and combining it with complementary information from $\mu \rightarrow e\gamma$ and $\mu \rightarrow 3e$, it becomes possible to disentangle different underlying sources of LFV [19–22], in particular given the projected limits on these $\mu \rightarrow e$ transitions from the next generation of experiments, which will constitute the most stringent bounds on LFV interactions ever conceived.

The current leading limits on the purely leptonic channels are $\text{Br}[\mu \rightarrow e\gamma] < 4.2 \times 10^{-13}$ [23] and $\text{Br}[\mu \rightarrow 3e] < 1.0 \times 10^{-12}$ [24] (here and below at 90% confidence level), which are set to improve at MEG II [25] and Mu3e [26], respectively (and potentially beyond [27]). For $\mu \rightarrow e$ conversion in nuclei, the current limits are given by the

SINDRUM-II experiment as

$$\text{Br}[\mu \rightarrow e, \text{Ti}] < 6.1 \times 10^{-13} \quad [28],$$

$$\text{Br}[\mu \rightarrow e, \text{Au}] < 7 \times 10^{-13} \quad [29], \quad (1)$$

measured on titanium and gold targets, respectively,¹ and with improvements of up to four orders of magnitude projected for the upcoming experiments of Mu2e [32] and COMET [33] on aluminum targets.

To infer implications regarding the underlying LFV interactions from such limits in a robust manner, it is crucial to fully control and quantify uncertainties at each step of the theoretical description, in particular for the nonperturbative inputs of hadronic and nuclear matrix elements as well as Coulomb corrections. The nuclear response functions are particularly intricate, especially those related to the couplings to neutrons as they are not directly constrained by experiment. Only recently, direct insights into neutron densities of a few selected nuclei became available via parity-violating electron scattering (PVES) [34–36]. In this work, we address the shortcomings of previously unquantified uncertainties for the nuclear structure input by exploiting strong correlations among charge, proton, and neutron matrix elements from ab initio calculations using the in-medium similarity renormalization group (IMSRG) [37–41] with state-of-the-art interactions from chiral EFT [42–46].

¹ Conventionally, these limits are normalized to muon capture [30]. The earlier limit $\text{Br}[\mu \rightarrow e, \text{Ti}] < 4.3 \times 10^{-12}$ [31] is superseded by Ref. [28] as the final result from the SINDRUM-II experiment.

The leading contributions to $\mu \rightarrow e$ conversion originate from scalar, vector, and dipole interactions, which couple in a spin-independent (SI) way to the nucleus and thus show a coherent enhancement with the number of nucleons in the nucleus. The SI $\mu \rightarrow e$ conversion rate is conventionally expressed in terms of so-called overlap integrals [1], labeled as $S^{(N)}$, $V^{(N)}$, and D , with $N = n, p$, according to

$$\Gamma_{\mu \rightarrow e}^{\text{SI}} = \frac{4m_{\mu}^5}{\Gamma_{\text{cap}}} \sum_{Y=L,R} \left| \sum_{I_i} \bar{C}_Y^{I_i} I_i \right|^2, \quad (2)$$

with the muon capture rate Γ_{cap} and where I_i runs over all overlap integrals. The prefactors $\bar{C}_Y^{I_i}$ are given as a combination of Wilson coefficients and hadronic matrix elements as defined in Ref. [9] and summarized in App. D.

Obtaining fully quantified ab initio uncertainties for these overlap integrals is challenging, given the direct sensitivity to proton ρ_p , neutron ρ_n , or charge distributions ρ_{ch} [see Eq. (3) below]. Furthermore, due to Coulomb distortions of the lepton wave functions, uncertainties in the nuclear charge distribution ρ_{ch} also propagate in an indirect way [see Eq. (D5)]. The latter aspect was recently addressed by an improved extraction of charge distributions from elastic electron–nucleus scattering including statistical and systematic uncertainty estimates and correlations [12]. Using these results, quantified uncertainties for the dipole overlap integrals D for the nuclei considered could already be provided. In this work, we now address the uncertainties originating from the proton and neutron distributions ρ_p and ρ_n as well as the correlations among the various overlap integrals.

We focus the numerical analysis on the isotopes ^{27}Al , to be used in the upcoming Mu2e and COMET experiments, and ^{48}Ti , with 73.72% by far the most abundant titanium isotope and thus relevant for the previous SINDRUM-II experiment. In addition, we consider ^{48}Ca , which is both a valuable benchmark for nuclear structure calculations [47, 48], is relevant in the context of PVES [36], and whose charge distribution was measured precisely in electron scattering experiments.

II. AB INITIO CALCULATIONS

Ab initio calculations of nuclei are now able to simulate systems as heavy as ^{208}Pb [45, 46, 49–51], provide a global description of medium-mass nuclei including deformation [41, 52–54], and compute nuclear responses necessary for a microscopic description of fundamental interactions in nuclei [55–60]. We employ nuclear forces from chiral EFT rooted in QCD [61, 62]. Such forces are inherently uncertain due to truncations in the EFT, unknown short-range couplings that must be fit to data, and residual regularization scale and scheme dependence. To systematically explore this uncertainty, we consider a large ensemble of Hamiltonians consisting of nucleon–nucleon (NN) and three-nucleon ($3N$) potentials that

differ in their construction within chiral EFT, their regularization scale, and how they are fit to data. These include Hamiltonians fit only to two-, three-, and four-nucleon systems [42], Hamiltonians additionally optimized to bulk properties of medium-light nuclei and nuclear matter [43, 44, 46], and an ensemble of Hamiltonians constructed using a history matching procedure based on two- through four-nucleon systems and ^{16}O [45].

We compute the structure of nuclei by solving the many-body Schrödinger equation using the IMSRG [37, 38]. The IMSRG solves for a unitary transformation of the Hamiltonian $U = e^{\Omega}$ to either directly decouple the ground state from its excitations or alternatively to decouple a core and valence space from the rest of the Hilbert space via the valence-space IMSRG (VS-IMSRG) [39, 40], leaving a problem that can be solved using shell-model techniques. We truncate our (VS-)IMSRG calculations at the level of normal-ordered two-body operators, the (VS-)IMSRG(2), an approximation that has been demonstrated to be very reliable for ground-state properties of medium-mass nuclei [38, 48, 63]. All our calculations are performed in an optimized hybrid Hartree–Fock and natural orbital basis following the construction of Ref. [48], expanded in a basis of 15 major harmonic oscillator shells (with harmonic oscillator frequency $\hbar\omega = 16$ MeV) before being truncated to an effective model-space size of 11 major shells. We find the effects of relaxing this truncation to be negligible, indicating that our calculations are converged with respect to model-space size.

Ground-state expectation values of other operators are computed consistently by applying the same unitary transformation. We compute charge radii based on the point-proton radius operator and the spin-orbit correction [47, 48], and we compute the nuclear responses using the $M_{p/n}$ and $\Phi''_{p/n}$ multipole operators from Refs. [60, 64, 65]. Both our radius operators and our responses are made translationally invariant through consistent center-of-mass corrections [47, 66, 67], meaning the densities computed as Fourier transforms from our responses give the same $\langle r^2 \rangle$ values as the expectation values of our radius operators. More details on the many-body calculations are provided in Apps. A and B.

III. OVERLAP INTEGRALS

The overlap integrals in Eq. (2) can be expressed as

$$\begin{aligned} I_0 &\equiv D = -\frac{4}{\sqrt{2} m_{\mu}^{3/2}} \int_0^{\infty} dr E(r) d(r), \\ I_{1,2} &\equiv S^{(N)} = \frac{\#N}{2\sqrt{2} m_{\mu}^{5/2}} \int_0^{\infty} dr \rho_N(r) s(r), \\ I_{3,4} &\equiv V^{(N)} = \frac{\#N}{2\sqrt{2} m_{\mu}^{5/2}} \int_0^{\infty} dr \rho_N(r) v(r), \end{aligned} \quad (3)$$

where $\rho_N(r)$ refers to the proton/neutron distribution normalized to 1 with $\#N = Z, A - Z$ for $N = p, n$,

respectively, and we put the electron mass m_e to zero (see Ref. [12] for overlap integrals with finite m_e). $E(r)$ denotes the electric field of the nucleus, which can be calculated based on the charge distribution ρ_{ch} , and $s(r)$, $v(r)$, $d(r)$ are combinations of the radial parts of the muon and electron wave functions, which are obtained by numerically solving the Dirac equation with a radial potential given by the electric field. For definitions of these quantities we refer to App. D and Refs. [12, 13].

Direct calculations of these overlap integrals are challenging, especially for the neutron responses involving ρ_n , as phenomenological approaches employ uncontrolled approximations and current ab initio calculations have considerable uncertainties due to the EFT truncation of the Hamiltonian. In ab initio calculations, however, these uncertainties are controlled and understood to be strongly correlated in related observables [47, 48, 56], which we leverage by computing the structure of ^{27}Al , ^{48}Ca , and ^{48}Ti for a broad set of chiral EFT Hamiltonians. We find strong correlations among charge, point-proton, and point-neutron distributions [47, 56] and exploit these to obtain robust results for the scalar and vector overlap integrals. As a reference point, we employ the charge densities $\rho_{\text{ch}}^{\text{ref}}$ and resulting charge radii squared $\langle r^2 \rangle_{\text{ch}}^{\text{ref}}$ as extracted from elastic electron scattering in Ref. [12].

Figure 1 shows these correlations between the scalar and vector overlap integrals and the charge radius squared for the three isotopes considered. In each case, a very clear linear relation is observed, which we fit with a simple linear regression according to

$$I_i(\langle r^2 \rangle_{\text{ch}}) = m_i \left(\langle r^2 \rangle_{\text{ch}} - \langle r^2 \rangle_{\text{ch}}^{\text{ref}} \right) + b_i. \quad (4)$$

We shift the x -axis to be centered around the reference charge radius squared in such a way that $I_i(\langle r^2 \rangle_{\text{ch}}^{\text{ref}}) = b_i$ and the influence of the correlation between m_i and b_i on the result is minimized. We propagate uncertainties based on the input charge radius squared as well as the fit residuals as discussed in more detail in App. C. The uncertainty from the fit residuals is reflective of remaining uncorrelated EFT uncertainties in our nuclear structure calculations. Additionally, we tested our model-space and many-body uncertainties by performing calculations in larger model spaces and using the IMSRG(3)- N^7 truncation [48, 73], respectively, for a few Hamiltonians in ^{48}Ca and found that these results also lie perfectly within our established correlations. Based on the extracted charge radii from Ref. [12], we find for the overlap integrals the values in Table I, reasonably consistent with the results from Ref. [1], but, crucially, including explicit uncertainty estimates.

We also determine the correlations among the different overlap integrals with respect to both uncertainty components given in Table I. For the uncertainties due to the distributions of the residuals in the correlation, we calculate the pairwise correlation between two residual distributions. For the uncertainties due to the charge radius, we propagate the correlations of the parameters

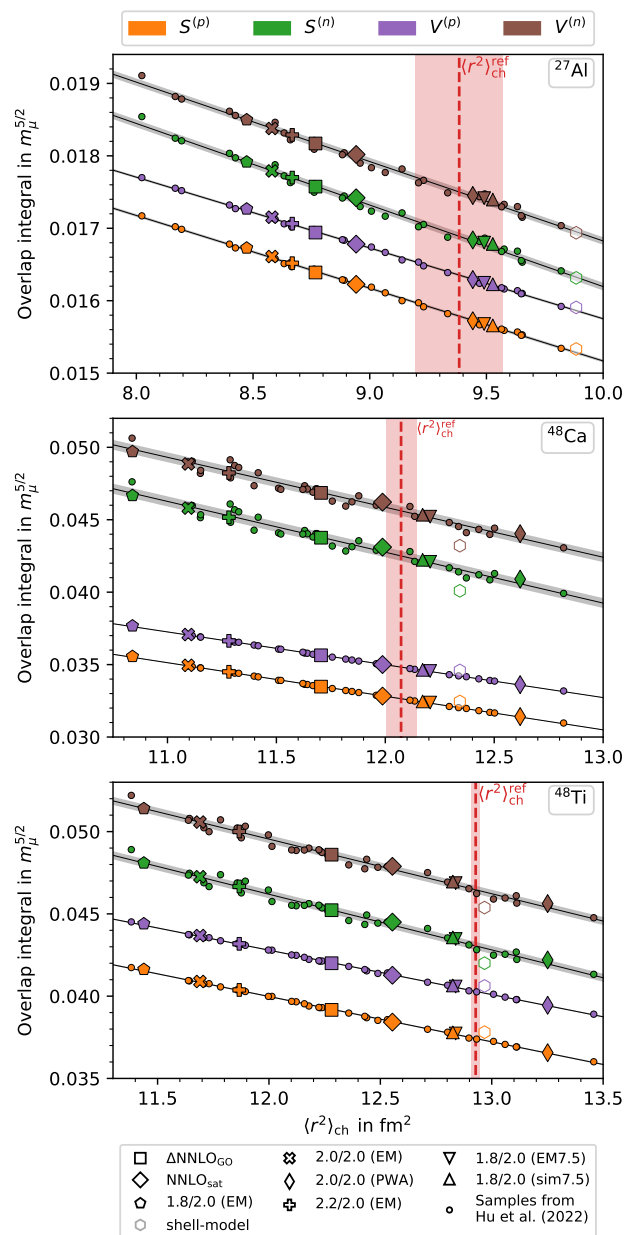


FIG. 1. Correlations between $\langle r^2 \rangle_{\text{ch}}$ and the overlap integrals from Eq. (3) using the IMSRG (specifically VS-IMSRG for ^{27}Al , ^{48}Ti) based on a representative set of chiral Hamiltonians (see App. A for details). The shell-model results, based on Refs. [9, 68–72], are shown for comparison and are not included in the correlation analysis.

of ρ_{ch} , which allows us to quantify the correlations with the dipole overlap integrals as well. Since for $i = 1-4$ the overlap integrals are all linearly dependent on the same charge radius squared $\langle r^2 \rangle_{\text{ch}}$, the overlap integrals I_1 to I_4 are pairwise maximally correlated for the latter uncertainty component. Table II shows the combined correlations of both components, clearly displaying the stronger correlations between charge and proton responses

I_i	This work/[12]	[1]
D	0.0359(2)	0.0362
$S^{(p)}$	0.01579(2)(19)	0.0155
^{27}Al $S^{(n)}$	0.01689(5)(21)	0.0167
$V^{(p)}$	0.01635(2)(18)	0.0161
$V^{(n)}$	0.01750(5)(21)	0.0173
D	0.07479(10)	–
$S^{(p)}$	0.03265(03)(16)	–
^{48}Ca $S^{(n)}$	0.04250(34)(25)	–
$V^{(p)}$	0.03483(02)(16)	–
$V^{(n)}$	0.04561(34)(24)	–
D	0.08640(11)	0.0864
$S^{(p)}$	0.03742(05)(5)	0.0368
^{48}Ti $S^{(n)}$	0.04305(25)(6)	0.0435
$V^{(p)}$	0.04029(04)(5)	0.0396
$V^{(n)}$	0.04646(24)(5)	0.0468

TABLE I. Overlap integrals as a result of the correlation analysis in Fig. 1. The values for the dipole overlap integral D are taken from Ref. [12] with the therein quoted total uncertainty. For the other overlap integrals, the first uncertainty component quantifies the remaining EFT uncertainties based on the correlation, see App. C, and the second one is propagated from the reference charge radius squared [12].

and weaker but still sizable correlations between them and the neutron responses. Since the total correlations are a weighted combination of the two uncertainty components, the absolute value of the correlation is strongly dependent on their relative size. If the propagated input uncertainties dominate as in ^{27}Al , the correlations are significantly stronger than in cases in which the fit uncertainties dominate as in ^{48}Ti , since those are statistically more independent.

IV. NEUTRON SKIN

Our work allows us to predict weak scattering in nuclei in a controlled and precise way. To test our predictions against existing weak-scattering data, we exploit the same correlations among the charge radius squared and the point-proton, point-neutron, and weak radius squared to extract values for these radii based on the input radius $\langle r_{\text{ch}}^2 \rangle^{\text{ref}}$ from Ref. [12]. We compare the resulting neutron and weak skin thickness to the results from the PVES experiments Q_{weak} on ^{27}Al [35] and CREX on ^{48}Ca [36] as shown in Table III (for individual radii and results for ^{48}Ti see Table V). We find mostly consistent values with some very slight tensions, which mostly trace back to different input values for the charge radius. We also compare to the correlation analysis of Ref. [47], which shows good consistency despite a much smaller set of chiral interactions and the use of a large proton radius in

^{27}Al					
	D	$S^{(p)}$	$S^{(n)}$	$V^{(p)}$	$V^{(n)}$
D	1.0000	0.7205	0.7030	0.7210	0.7028
$S^{(p)}$		1.0000	0.9656	1.0000	0.9645
$S^{(n)}$			1.0000	0.9664	1.0000
$V^{(p)}$				1.0000	0.9654
$V^{(n)}$					1.0000
^{48}Ca					
	D	$S^{(p)}$	$S^{(n)}$	$V^{(p)}$	$V^{(n)}$
D	1.0000	0.8938	0.5295	0.8956	0.5272
$S^{(p)}$		1.0000	0.6125	0.9999	0.6089
$S^{(n)}$			1.0000	0.6120	0.9999
$V^{(p)}$				1.0000	0.6085
$V^{(n)}$					1.0000
^{48}Ti					
	D	$S^{(p)}$	$S^{(n)}$	$V^{(p)}$	$V^{(n)}$
D	1.0000	0.4657	0.1169	0.5003	0.1163
$S^{(p)}$		1.0000	0.1118	0.9991	0.0916
$S^{(n)}$			1.0000	0.1176	0.9997
$V^{(p)}$				1.0000	0.0978
$V^{(n)}$					1.0000

TABLE II. Total correlations among the different overlap integrals as a combination of the propagated correlations from the observed correlations among the fit residuals and the reference charge density. The number of digits quoted does not represent precision but is chosen for reproducibility such that the eigenvalues of the correlation matrix remain non-negative.

the conversion between charge and point-proton radii [65]. We emphasize that through the use of a large ensemble of Hamiltonians and a detailed correlation analysis including also many-body uncertainties we improve upon past work and are able to make substantially more precise predictions for weak-scattering properties. This can further refine the analysis and interpretation of PVES experiments.

PVES experiments measure the left–right asymmetry [34–36], which becomes proportional to the weak form factor at the respective momentum transfer only in the plane-wave limit, while a rigorous extraction requires the consideration of Coulomb corrections. As the weak density is not fully known, this inevitably introduces some model dependence. For this reason, we also considered the direct correlation between charge and weak form factor at the momentum transfer of the experiment, using as reference value the form factor calculated via the charge distribution from Ref. [12]. The resulting values are also listed in Table III, together with the respective results from Q_{weak} and CREX.

For ^{27}Al our result is roughly 8% smaller than the ex-

		This work/[12]	References
^{27}Al	$r_n - r_p$ [fm]	0.021(09)(46)	-0.04(12) [35]
	$r_w - r_{\text{ch}}$ [fm]	0.023(10)(44)	-0.04(15) [35]
	$F_{\text{ch}}^{\text{exp}}$	0.3665(45)	0.382(12) [35]
	F_w^{exp}	0.3614(23)(46)	0.393(38) [35]
^{48}Ca	$r_n - r_p$ [fm]	0.152(17)(15)	[0.12, 0.15] [47] 0.121(26)(24) [36]
	$r_w - r_{\text{ch}}$ [fm]	0.191(18)(15)	0.159(26)(23) [36]
	$F_{\text{ch}}^{\text{exp}}$	0.15603(55)	0.1581 [36]
	F_w^{exp}	0.1171(28)(5)	0.1304(52)(20) [36]

TABLE III. Neutron and weak skin calculated as the difference between the respective radii that were correlated to the charge radius (for individual radii and the results for ^{48}Ti see Table V). We also considered correlating the radius differences directly, leading to identical central values, but a reduced sensitivity to the reference charge radius. We further provide the charge and weak form factor at the momentum transfer used by the respective PVES experiments $F_{\text{ch,w}}^{\text{exp}} = F_{\text{ch,w}}(q_{\text{exp}})$ with $q_{\text{exp}} = 0.87335(58) \text{ fm}^{-1}$ [36] for ^{48}Ca and $q_{\text{exp}} = 0.77802(33) \text{ fm}^{-1}$ [35] for ^{27}Al . The uncertainties propagated from the spread in the momentum are not listed in the table, but amount to roughly 0.0005 for CREX and 0.0004 for Q_{weak} in the quoted weak form factors. In all cases the first uncertainty component quantifies the remaining EFT uncertainties based on the correlation, see App. C, and the second one is propagated from the reference charge radius squared [12].

perimental one, which is amply covered by the $\simeq 10\%$ uncertainty on the experimental value and can be attributed, to a large part, to the smaller charge form factor used as input. For ^{48}Ca the difference is a bit larger and the experimental uncertainty is significantly smaller, such that at face value we see a tension around 2σ . However, part of the tension again originates from different input for the charge form factor. Further, if we calculate the left-right asymmetry (including Coulomb corrections) based on our reference charge density and the extracted weak density from App. E, we find an asymmetry that comes significantly closer to the experimental result, reducing the mismatch to about 1σ . This observation suggests that the result for the weak form factor as extracted by CREX might depend more strongly on the details of the calculation of the Coulomb corrections than assumed in Ref. [36].

V. CONCLUSIONS

In this work, we calculated the overlap integrals for $\mu \rightarrow e$ conversion in nuclei corresponding to the leading SI responses using ab initio methods, providing, for the first time, robust uncertainty estimates including correlations among the different integrals. To this end, we explored correlations among the overlap integrals and the nuclear charge radius for the phenomenologically most relevant

isotopes ^{27}Al and ^{48}Ti as well as ^{48}Ca , the latter allowing for validation against previous work and data from PVES. As our main result, see Fig. 1, we observe that tight correlations exist even for the neutron responses, covering both a variety of chiral Hamiltonians and many-body uncertainties and thereby leading to much more stringent constraints than in previous work. Based on our results, it is now possible to propagate nuclear uncertainties in the evaluation of the $\mu \rightarrow e$ conversion rate in Eq. (2), crucial for any robust assessment of the sensitivity to different underlying LFV mechanisms. Similar strategies will allow for improved calculations of nuclear matrix elements for PVES, coherent neutrino-nucleus scattering [74, 75], and the direct detection of dark matter [76, 77].

ACKNOWLEDGMENTS

We thank Baishan Hu for valuable discussions. Financial support by the Swiss National Science Foundation (Project No. TMCG-2.213690) is gratefully acknowledged. This work was supported in part by the European Research Council (ERC) under the European Union’s Horizon 2020 research and innovation programme (Grant Agreement No. 101020842), by the U.S. Department of Energy, Office of Science, Office of Advanced Scientific Computing Research and Office of Nuclear Physics, Scientific Discovery through Advanced Computing (SciDAC) program (SciDAC-5 NUCLEI), by the Laboratory Directed Research and Development Program of Oak Ridge National Laboratory, managed by UT-Battelle, LLC, for the U.S. Department of Energy, and by JST ERATO Grant No. JPMJER2304, Japan. This research used resources of the Oak Ridge Leadership Computing Facility located at Oak Ridge National Laboratory, which is supported by the Office of Science of the Department of Energy under contract No. DE-AC05-00OR22725. The authors gratefully acknowledge the Gauss Centre for Supercomputing e.V. (www.gauss-centre.eu) for funding this project by providing computing time through the John von Neumann Institute for Computing (NIC) on the GCS Supercomputer JUWELS at Jülich Supercomputing Centre (JSC).

Appendix A: Ensemble of nuclear Hamiltonians

We use an ensemble of Hamiltonians with NN and $3N$ potentials from chiral EFT in our (VS-)IMSRG calculations to explore EFT truncation uncertainties. The Hamiltonians we employ vary in their truncation order, their regularization cutoff scales, details of their EFT construction, and how they are fit to data. All Hamiltonians are fit to NN scattering data, deuteron properties, and properties of few-body systems with $A \leq 4$, but some are optimized against additional constraints. The long-range parts are constrained using low-energy constants determined from pion-nucleon scattering [78–

Name	Ref.	Order, Cutoff		λ	Optimize to $A > 4$?
		NN	$3N$		
1.8/2.0 (EM)				1.8	
2.0/2.0 (EM)	[42]	N^3LO , 500	N^2LO , 394	2.0	No
2.2/2.0 (EM)				2.2	
2.0/2.0 (PWA)				2.0	
1.8/2.0 (EM7.5)	[46]	N^3LO , 500	N^2LO , 394	1.8	Yes
1.8/2.0 (sim7.5)		N^2LO , 550		1.8	
$NNLO_{\text{sat}}$	[43]	N^2LO , 450	N^2LO , 450	–	Yes
$\Delta NNLO_{GO}^b$	[44]	N^2LO , 394	N^2LO , 394	–	Yes ^a
34 samples from Hu et al. ^b	[45]	N^2LO , 394	N^2LO , 394	–	Yes

^a Fit to nuclear matter properties.

^b Explicit inclusion of Δ isobars in EFT construction.

TABLE IV. Nuclear Hamiltonians from chiral EFT used in this work and in Fig. 1. Regulator cutoffs are given in MeV. SRG resolution scales λ are given in fm^{-1} where relevant. Hamiltonians optimized to $A > 4$ are generally fit to ground-state energies and charge radii of ^{16}O , but occasionally also selected ground-state energies and charge radii of other nuclei such as ^{14}C and $^{22,24,25}\text{O}$.

80]. Furthermore, some Hamiltonians are transformed to lower resolution scales using the similarity renormalization group (SRG) [81], making them more perturbative and amenable to many-body calculations.

An overview of all 42 nuclear Hamiltonians we use is given in Table IV [42–46]. They are generally at next-to-next-to-leading order (N^2LO), but selected Hamiltonians have NN interactions at one order higher, N^3LO . The Hamiltonians from Refs. [44, 45] explicitly include Δ isobars in their chiral EFT construction. Regulator cutoffs range from 394 to 550 MeV, and low-resolution Hamiltonians with SRG resolution scales from $\lambda = 1.8$ to 2.2 fm^{-1} are explored. The 34 interactions of Ref. [45] are samples from distributions of LECs determined through a history matching procedure comparing against NN scattering data, deuteron properties, ground-state energies and charge radii of few-body systems with $A \leq 4$, and the ground-state energy and charge radius of ^{16}O , capturing the uncertainty in nuclear Hamiltonians through uncertainties in the underlying LECs.² The broad range of Hamiltonians we consider allows us to probe many aspects of the chiral EFT truncation uncertainty, and the strong correlations we find apply to all interactions, indicating that exploiting such correlations is insensitive to specific details of the Hamiltonian construction.

² For our calculations of ^{27}Al , we find that six of the 34 samples from Ref. [45] give unphysical results in our calculations. These are not shown and excluded from our analysis.

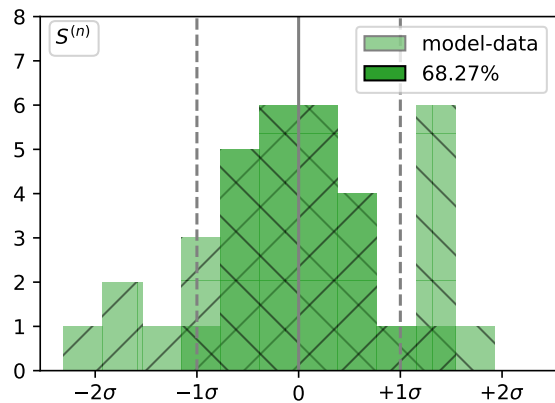


FIG. 2. Residual distribution for the $S^{(n)}$ overlap integral of ^{27}Al .

Appendix B: Many-body uncertainties

In addition to the EFT uncertainties explored by our ensemble of Hamiltonians, ab initio many-body calculations also have model-space uncertainties due to working in a finite basis and many-body uncertainties due to truncations in the many-body method. For the 1.8/2.0 (EM), $NNLO_{\text{sat}}$, and 1.8/2.0 (EM7.5) Hamiltonians, we explored these uncertainties in ^{48}Ca by increasing our model-space size to 13 effective harmonic oscillator shells and by performing $\text{IMSRG}(3)\text{-}N^7$ calculations with restricted normal-ordered three-body operators [48], improving on the $\text{IMSRG}(2)$ truncation we employ for the rest of this work. For both the larger model-space size and the more precise $\text{IMSRG}(3)\text{-}N^7$ truncation, the resulting charge radii and overlap integrals in Fig. 1 shift by small amounts essentially exactly along the linear correlations we find. This indicates that many-body uncertainties are similarly correlated in ab initio calculations of point-proton, point-neutron, and charge densities. Specifically, the correlations we find can be applied without considering additional uncorrelated uncertainties due to truncations and approximations in our (VS-)IMSRG calculations.

Appendix C: Details of correlation analysis

The correlation analysis employs a linear fit according to Eq. (4) using the Levenberg–Marquardt method [82, 83] as implemented by the `python` package `lmfit` [84]. We consider two uncertainty components: one propagated from the input quantities and one based on the fit quality. The former is straightforward to implement, using the uncertainty of $\langle r^2 \rangle_{\text{ch}}^{\text{ref}}$ coming from the parameterization of $\rho_{\text{ch}}^{\text{ref}}$, and propagating it according to Eq. (4).³

³ We follow the preferred strategy for the estimate of systematic uncertainties as argued in Ref. [12]. This implies that for ^{48}Ti the

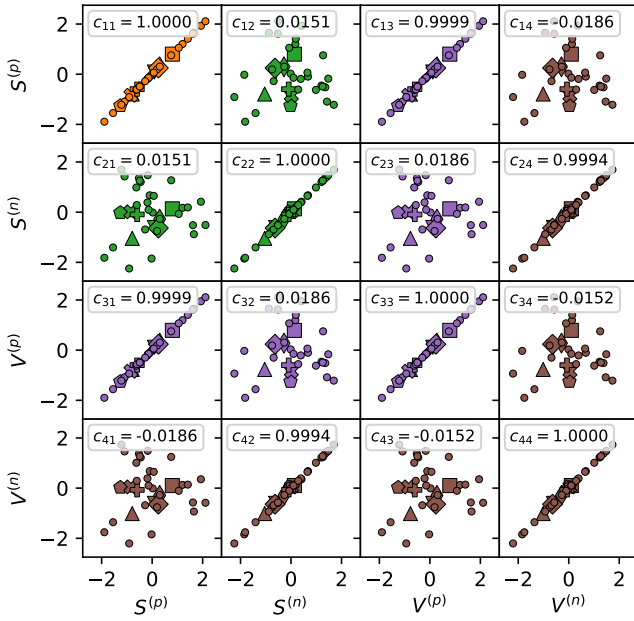


FIG. 3. Correlations of the residuals for ^{27}Al normalized to the uncertainty based on the distribution as shown in Fig. 2, using the same symbols as in Fig. 1. c_{ij} refers to the correlation between the residuals of I_i and I_j .

For the latter, an uncertainty estimate solely based on the fit statistics will inevitably grossly underestimate the resulting uncertainties, particularly if the uncertainties of the individual data points are unknown and sizable correlations among different results from the same chiral EFT scheme cannot be included systematically. For this reason, we estimate the uncertainty of the b_i , and thus the overlap integrals based on the distribution of the residuals, in such a way that $\Delta I_i = \Delta b_i$ is given by the standard deviation of all residuals of the fit. Figure 2 shows exemplarily such a residual distribution for the $S^{(n)}$ overlap integral for ^{27}Al and confirms that the resulting 1σ uncertainties are reasonable. The correlations of this uncertainty component among the different overlap integrals can be calculated with statistical methods based on the different residual distributions. We find the correlations as illustrated in Fig. 3 for ^{27}Al , which shows the observed strong correlation between overlap integrals that couple to the same nuclear density. This correlation is then combined with the propagated correlation from the input charge density parametrization, resulting in the values from Table II. We find similar behavior for the other nuclei studied in this work, see App. F.

result is more strongly constrained by the charge radius extracted from muon spectroscopy, in contrast to ^{27}Al and ^{48}Ca , in which cases the uncertainties assigned in Fig. 1 account for the tension observed between scattering data and spectroscopy as well.

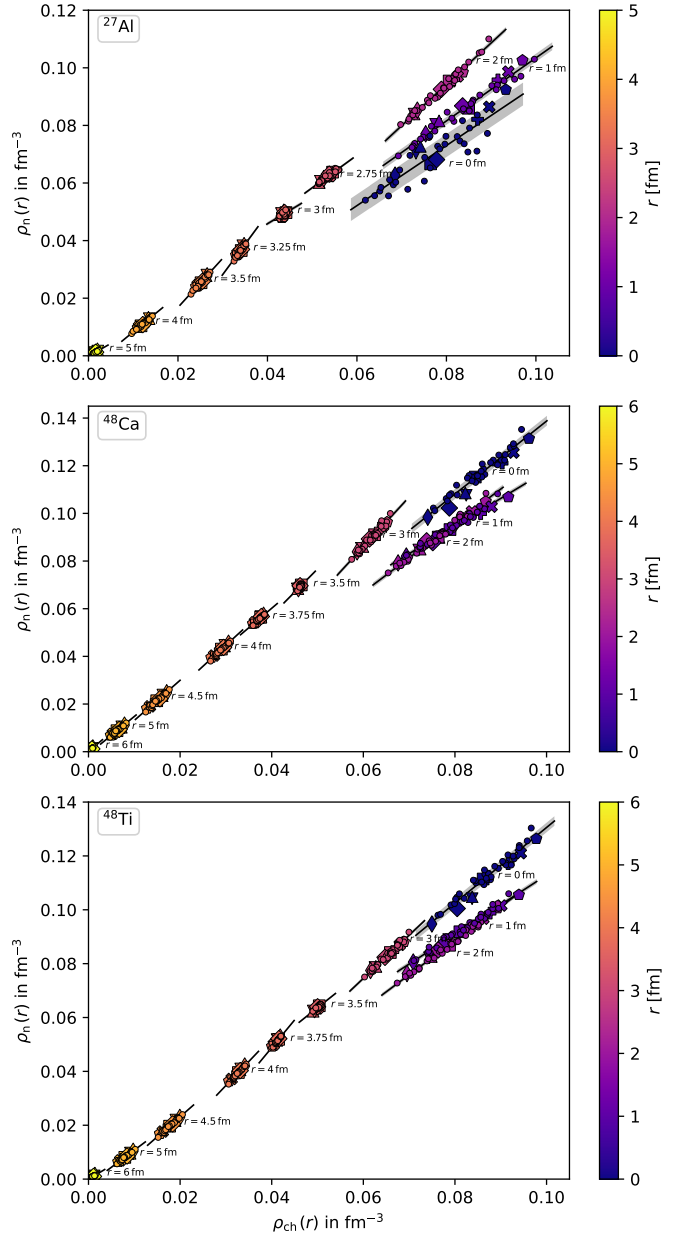


FIG. 4. Correlations between ρ_{ch} and ρ_n illustrated for selected values of r for ^{27}Al , ^{48}Ca , and ^{48}Ti . Symbols are as in Fig. 1

Appendix D: $\mu \rightarrow e$ conversion

The leading coherently enhanced contributions to $\mu \rightarrow e$ conversion come from scalar, vector, and dipole interactions. The relevant effective operators up to dimension seven are given by

$$\begin{aligned} \mathcal{L}_{\text{eff}}^{\text{SI}} = & \frac{1}{\Lambda^2} \sum_{\substack{Y=L,R \\ q=u,d,s}} \left[C_Y^{S,q} (\bar{e}_Y \mu) (\bar{q} q) + C_Y^{V,q} (\bar{e}_Y \gamma^\mu \mu) (\bar{q} \gamma_\mu q) \right] \\ & + \frac{1}{\Lambda} \sum_{Y=L,R} C_Y^D (\bar{e}_Y \sigma^{\mu\nu} \mu) F_{\mu\nu} \end{aligned}$$

$$+ \frac{\alpha_s}{\Lambda^3} \sum_{Y=L,R} C_Y^{GG}(\bar{e}_Y \mu)(G_{\alpha\beta}^a G_a^{\alpha\beta}) + \text{h.c.}, \quad (\text{D1})$$

where we use $\bar{e}_Y = \overline{eP_Y} = \bar{e}P_Y$ with $Y \in \{L, R\}$ and $P_{L/R} = (\mathbb{1} \mp \gamma_5)/2$. This convention makes the decoupling of the left-handed and right-handed components of the electron for $m_e \rightarrow 0$ explicit. We introduce the BSM scale Λ to make the Wilson coefficients $C_Y^{X,(q)}$ with $X = S, V, D, GG$ dimensionless. Using these conventions, the SI $\mu \rightarrow e$ conversion rate takes the form quoted in Eq. (2) with the prefactors given as [9]

$$\begin{aligned} \bar{C}_Y^{S^{(N)}} &= \frac{1}{\Lambda^2} \sum_q C_Y^{S,q} \frac{m_N}{m_q} f_q^N + \frac{4\pi}{\Lambda^3} C_Y^{GG} a_N, \\ \bar{C}_Y^{V^{(N)}} &= \frac{1}{\Lambda^2} \sum_q C_Y^{V,q} f_{V,q}^N, \\ \bar{C}_Y^D &= \frac{\eta_e}{4m_\mu \Lambda} C_Y^D, \end{aligned} \quad (\text{D2})$$

where η_e refers to the sign convention for the charge, corresponding to a minimal coupling of $D_\mu = \partial_\mu + i\eta_e \sqrt{4\pi\alpha_{\text{el}}} A^\mu$ [85], $\alpha_{\text{el}} = e^2/(4\pi)$, and the hadronic matrix elements defined by

$$\begin{aligned} \langle N | m_q \bar{q} q | N \rangle &= \bar{u}'_N [m_N f_q^N(q)] u_N, \\ \langle N | \bar{q} \gamma^\mu q | N \rangle &= \bar{u}'_N \left[\gamma^\mu F_1^{q,N}(q) - \frac{i\sigma^{\mu\nu} q_\nu}{2m_N} F_2^{q,N}(q) \right] u_N, \\ \langle N | G_{\mu\nu}^a G_a^{\mu\nu} | N \rangle &= \bar{u}'_N \left[\frac{4\pi}{\alpha_s} a_N(q) \right] u_N, \end{aligned} \quad (\text{D3})$$

with $\bar{u}_N = \bar{u}_N(p, s)$, $\bar{u}'_N = \bar{u}_N(p', s')$, momenta and spins of initial and final nucleon p, s and p', s' , and $q = p - p'$, see, e.g., Refs. [9, 65, 86, 87] for a review of the required matrix elements.

The overlap integrals are defined in Eq. (3), with the electric field of the nucleus given by

$$E(r) = \frac{\sqrt{4\pi\alpha_{\text{el}}}}{r^2} \int_0^r dr' r'^2 \rho_{\text{ch}}(r'), \quad (\text{D4})$$

in terms of the charge distribution ρ_{ch} . The combinations of the radial parts of the muon and electron wave functions are defined as

$$\begin{aligned} s(r) &= g_{-1}^e(r) g_{-1}^\mu(r) - f_{-1}^e(r) f_{-1}^\mu(r), \\ v(r) &= g_{-1}^e(r) g_{-1}^\mu(r) + f_{-1}^e(r) f_{-1}^\mu(r), \\ d(r) &= g_{-1}^e(r) f_{-1}^\mu(r) + f_{-1}^e(r) g_{-1}^\mu(r), \end{aligned} \quad (\text{D5})$$

where the full wave functions are decomposed as

$$\psi_\kappa^\mu(\mathbf{r}) = \frac{1}{r} \begin{pmatrix} g_\kappa(r) \phi_\kappa^\mu(\hat{\mathbf{r}}) \\ i f_\kappa(r) \phi_{-\kappa}^\mu(\hat{\mathbf{r}}) \end{pmatrix}, \quad (\text{D6})$$

separating the angular-momentum degrees of freedom into $\phi_\kappa^\mu(\hat{\mathbf{r}})$. The quantum numbers are contained in $\kappa \geq 0$ according to

$$j = |\kappa| - \frac{1}{2}, \quad j_z = \mu, \quad l = \begin{cases} \kappa & \kappa > 0, \\ -\kappa - 1 & \kappa < 0. \end{cases} \quad (\text{D7})$$

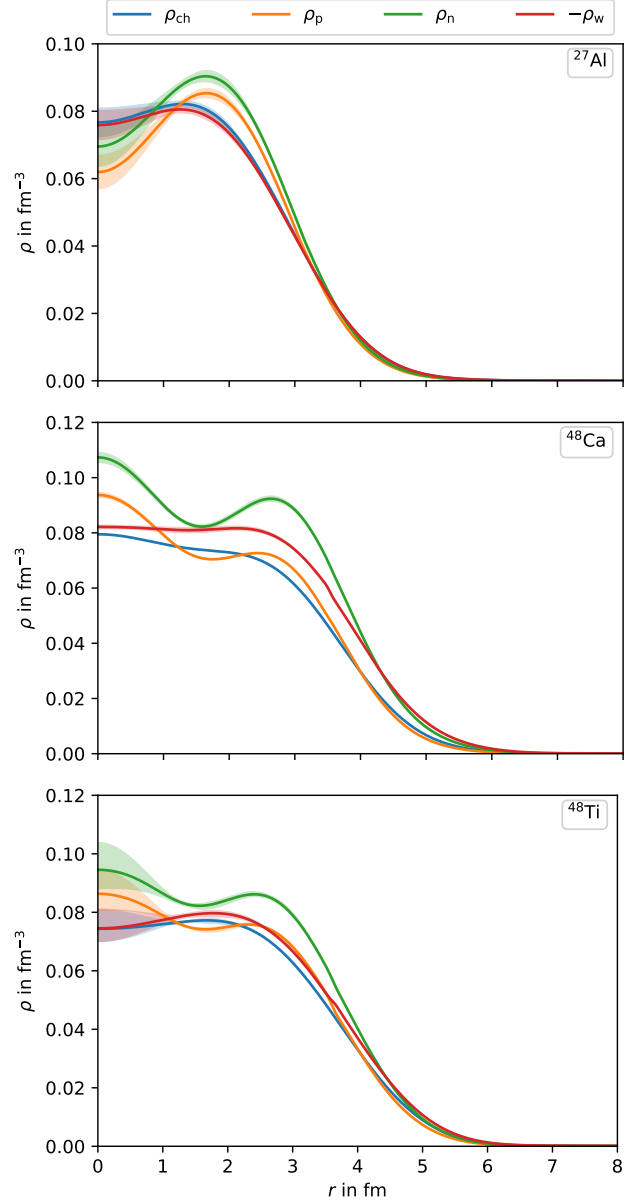
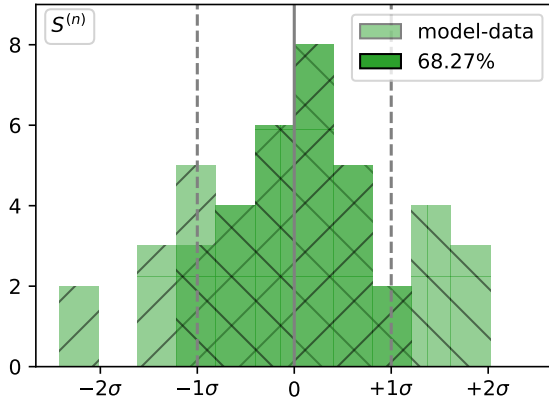
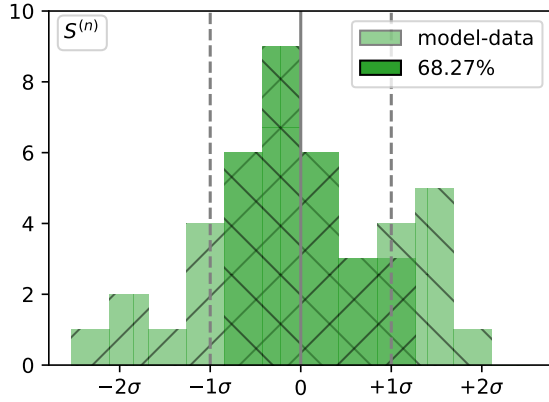


FIG. 5. Point-proton, point-neutron, and weak distributions for ^{27}Al , ^{48}Ca , and ^{48}Ti based on a correlation analysis at fixed r together with the input charge density; $\rho_{\text{ch}} = \rho_{\text{ch}}^{\text{ref}}$.

The radial potential of the nucleus necessary for solving the Dirac equation is given by the electric field as

$$V(r) = -\sqrt{4\pi\alpha_{\text{el}}} \int_r^\infty dr' E(r'). \quad (\text{D8})$$

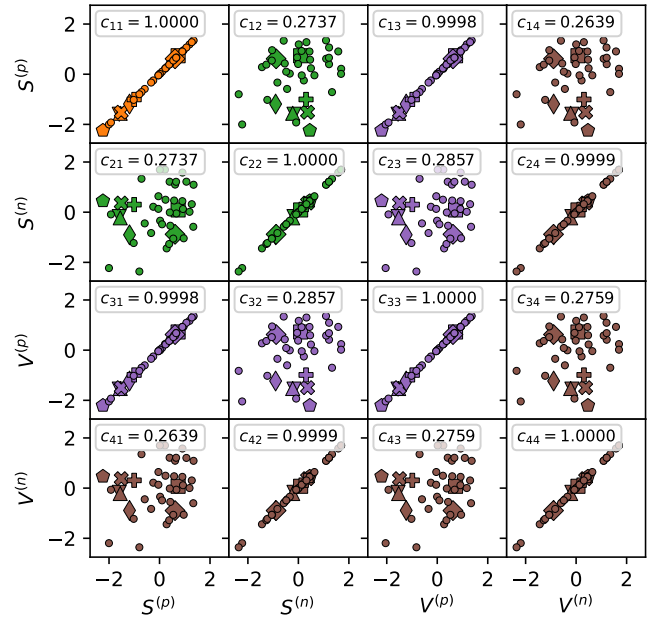
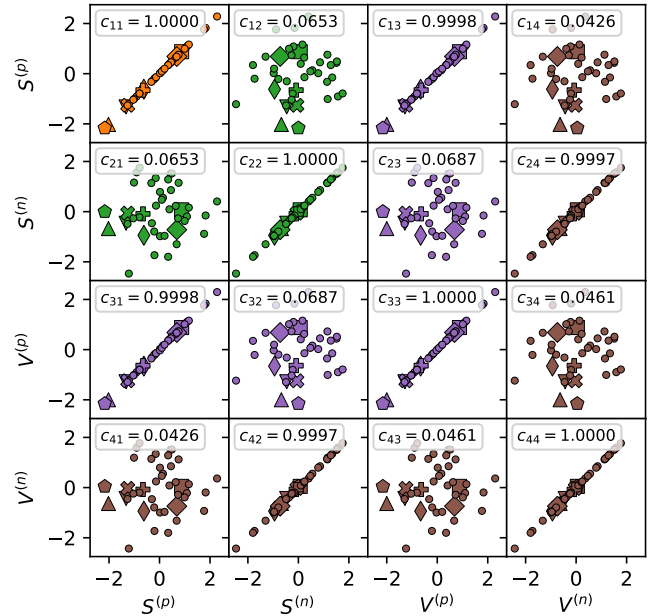
Again, we refer to Refs. [12, 13] for further details and conventions.

FIG. 6. Same as Fig. 2 for ^{48}Ca .FIG. 7. Same as Fig. 2 for ^{48}Ti .

Appendix E: Proton, neutron, and weak distributions

We can also perform the same correlation exercise individually between $\rho_{\text{ch}}(r)$ and $\rho_{\text{p}}(r)$, $\rho_{\text{n}}(r)$, or $\rho_{\text{w}}(r)$ directly. While this seems to work quite well empirically, we note that it is not clear that fitting the correlations at different r completely independently does not introduce additional systematic effects. Figure 4 shows the linear trend for a selection of values for r , scanning over the different interactions, for the correlation between $\rho_{\text{ch}}(r)$ and $\rho_{\text{n}}(r)$. With a fine sampling of r we can calculate distributions $\rho_{\text{p}}(r)$, $\rho_{\text{n}}(r)$, and $\rho_{\text{w}}(r)$ based on the extracted correlations and $\rho_{\text{ch}}^{\text{ref}}(r)$. We find the results shown in Fig. 5, where we included the uncertainties in the same way as for the overlap integrals. The uncertainties increase towards smaller radii, where the nucleus is probed less precisely experimentally. Moreover, as expected, the uncertainties for the weak and neutron distributions are larger than for the proton ones due to the higher uncertainties coming from the spread of the considered interactions. As a cross-check, we calculate the radii based on these distributions. We find, with a rough uncertainty estimate just based on the upper and lower error bands,

$$r_{\text{p}}^{27\text{Al}} = 3.0(2) \text{ fm}, \quad r_{\text{n}}^{27\text{Al}} = 3.0(2) \text{ fm},$$

FIG. 8. Same as Fig. 3 for ^{48}Ca .FIG. 9. Same as Fig. 3 for ^{48}Ti .

$$\begin{aligned} r_{\text{w}}^{27\text{Al}} &= 3.0(2) \text{ fm}, \\ r_{\text{p}}^{48\text{Ca}} &= 3.40(4) \text{ fm}, & r_{\text{n}}^{48\text{Ca}} &= 3.55(8) \text{ fm}, \\ r_{\text{w}}^{48\text{Ca}} &= 3.67(10) \text{ fm}, \\ r_{\text{p}}^{48\text{Ti}} &= 3.49(2) \text{ fm}, & r_{\text{n}}^{48\text{Ti}} &= 3.55(3) \text{ fm}, \\ r_{\text{w}}^{48\text{Ti}} &= 2.68(3) \text{ fm}, \end{aligned} \quad (\text{E1})$$

which are all consistent with the results from Table V, but give significantly larger uncertainties, due to the simple methodology of the uncertainty estimate here, for

		This work/[12]	References
^{27}Al	r_{ch}	[fm] 3.063(31)	3.035(2) [88] 3.0610(31) [89]
	r_{p}	[fm] 2.961(00)(32)	2.925(7) [35]
	r_{n}	[fm] 2.982(09)(33)	2.89(12) [35]
	r_{w}	[fm] 3.087(10)(32)	3.00(15) [35]
^{48}Ca	r_{ch}	[fm] 3.475(10)	3.451(9) [88] 3.4771(20) [89] 3.481 [36] 3.48(3) [47]
	r_{p}	[fm] 3.403(00)(10)	3.40(3)* [47]
	r_{n}	[fm] 3.555(17)(11)	[3.47, 3.60] [47]
	r_{w}	[fm] 3.665(18)(11)	[3.59, 3.71] [47]
	r_{ch}	[fm] 3.5955(25)	3.597(1) [88] 3.5921(17) [89]
	r_{p}	[fm] 3.515(00)(3)	
^{48}Ti	r_{n}	[fm] 3.568(12)(3)	
	r_{w}	[fm] 3.665(12)(3)	
	$r_{\text{n}} - r_{\text{p}}$	[fm] 0.053(12)(4)	
	$r_{\text{w}} - r_{\text{ch}}$	[fm] 0.070(12)(4)	

TABLE V. Extension to Table III, showing the absolute radii for ^{27}Al and ^{48}Ca (for $x \in \{\text{p}, \text{n}, \text{ch}, \text{w}\}$ we define $r_x = \sqrt{\langle r^2 \rangle_x}$) and the analogous results for ^{48}Ti , for which currently no experimental results from PVES exist. The values for the charge radius are taken from Ref. [12] and thus $r_{\text{ch}} = \sqrt{\langle r^2 \rangle_{\text{ch}}^{\text{ref}}}$. The asterisk indicates that this value is not given directly in Ref. [47], but can be inferred from the quantities provided.

which, in particular, the total charge was not constrained. Nevertheless, these values serve as a valuable crosscheck that the extracted distributions are meaningful.

Appendix F: Additional figures and tables

In this appendix, we provide further material for the isotopes not discussed in full detail in the main text. First, Figs. 6–9 show the residual distributions and their correlations for ^{48}Ca and ^{48}Ti . Table V extends Table III by absolute radii for ^{27}Al and ^{48}Ca and the analogous results for ^{48}Ti . The corresponding correlations, constructed in analogy to Fig. 1, are shown in Fig. 10.

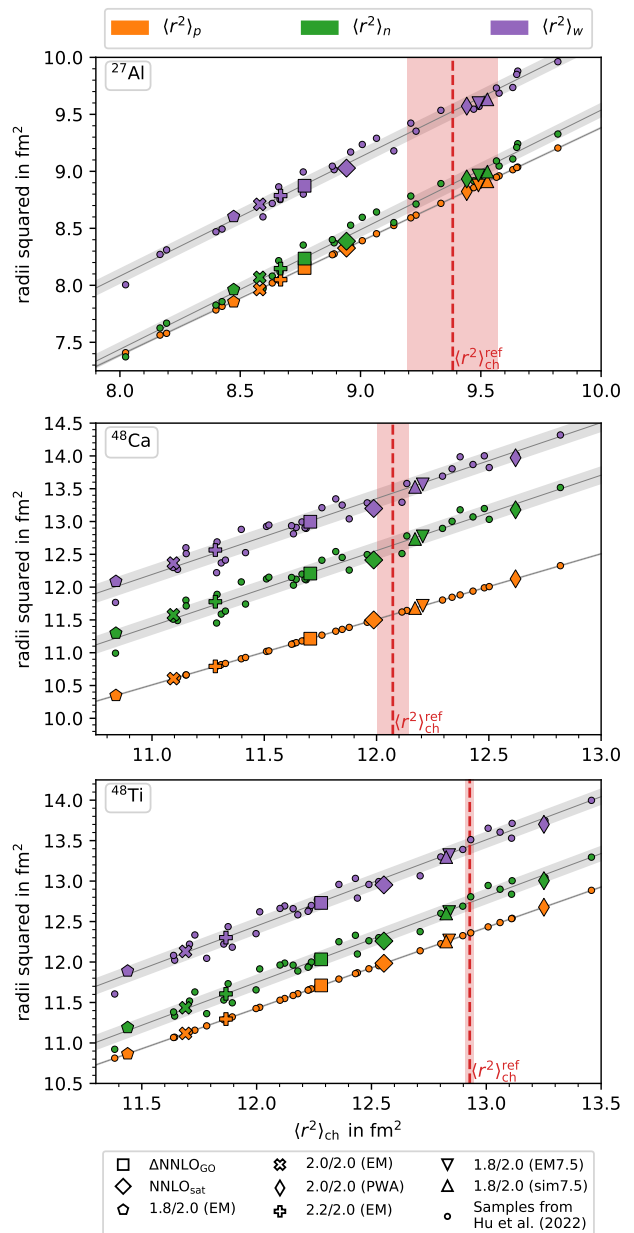


FIG. 10. Correlations between $\langle r^2 \rangle_{\text{ch}}$ and the point-proton, point-neutron, and weak radius squared, carried out in the same way as in Fig. 1.

- [1] R. Kitano, M. Koike, and Y. Okada, Phys. Rev. D **66**, 096002 (2002), [Erratum: Phys. Rev. D **76**, 059902 (2007)], arXiv:hep-ph/0203110.
[2] V. Cirigliano, R. Kitano, Y. Okada, and P. Tuzon, Phys. Rev. D **80**, 013002 (2009), arXiv:0904.0957.

- [3] A. A. Petrov and D. V. Zhuridov, Phys. Rev. D **89**, 033005 (2014), arXiv:1308.6561.
[4] A. Crivellin, S. Najjari, and J. Rosiek, J. High Energy Phys. **04**, 167 (2014), arXiv:1312.0634.
[5] A. Crivellin, M. Hoferichter, and M. Procura, Phys. Rev. D **89**, 093024 (2014), arXiv:1404.7134.

- [6] S. Davidson, Y. Kuno, and M. Yamanaka, *Phys. Lett. B* **790**, 380 (2019), arXiv:1810.01884.
- [7] E. Rule, W. C. Haxton, and K. McElvain, *Phys. Rev. Lett.* **130**, 131901 (2023), arXiv:2109.13503.
- [8] V. Cirigliano, K. Fuyuto, M. J. Ramsey-Musolf, and E. Rule, *Phys. Rev. C* **105**, 055504 (2022), arXiv:2203.09547.
- [9] M. Hoferichter, J. Menéndez, and F. Noël, *Phys. Rev. Lett.* **130**, 131902 (2023), arXiv:2204.06005.
- [10] W. C. Haxton, E. Rule, K. McElvain, and M. J. Ramsey-Musolf, *Phys. Rev. C* **107**, 035504 (2023), arXiv:2208.07945.
- [11] L. Borrel, D. G. Hitlin, and S. Middleton, arXiv:2401.15025.
- [12] F. Noël and M. Hoferichter, *J. High Energy Phys.* **08**, 052 (2024), arXiv:2406.06677.
- [13] F. Noël, $\mu \rightarrow e$ conversion in nuclei: *EFT description, charge densities, and pseudo-scalar decays*, Ph.D. thesis, Bern U. (2024).
- [14] W. Haxton, K. McElvain, T. Menzo, E. Rule, and J. Zupan, arXiv:2406.13818.
- [15] F. Delzanno, K. Fuyuto, S. González-Solís, and E. Mereghetti, arXiv:2411.13497.
- [16] A. Crivellin, S. Davidson, G. M. Pruna, and A. Signer, *J. High Energy Phys.* **05**, 117 (2017), arXiv:1702.03020.
- [17] V. Cirigliano, S. Davidson, and Y. Kuno, *Phys. Lett. B* **771**, 242 (2017), arXiv:1703.02057.
- [18] S. Davidson, Y. Kuno, and A. Saporta, *Eur. Phys. J. C* **78**, 109 (2018), arXiv:1710.06787.
- [19] S. Davidson, *J. High Energy Phys.* **02**, 172 (2021), arXiv:2010.00317.
- [20] S. Davidson and B. Echenard, *Eur. Phys. J. C* **82**, 836 (2022), arXiv:2204.00564.
- [21] M. Ardu, S. Davidson, and S. Lavignac, *J. High Energy Phys.* **11**, 101 (2023), arXiv:2308.16897.
- [22] M. Ardu, S. Davidson, and S. Lavignac, *Eur. Phys. J. C* **84**, 458 (2024), arXiv:2401.06214.
- [23] A. M. Baldini *et al.* (MEG), *Eur. Phys. J. C* **76**, 434 (2016), arXiv:1605.05081.
- [24] U. Bellgardt *et al.* (SINDRUM), *Nucl. Phys. B* **299**, 1 (1988).
- [25] A. M. Baldini *et al.* (MEG II), *Eur. Phys. J. C* **78**, 380 (2018), arXiv:1801.04688.
- [26] K. Arndt *et al.* (Mu3e), *Nucl. Instrum. Meth. A* **1014**, 165679 (2021), arXiv:2009.11690.
- [27] M. Aiba *et al.*, arXiv:2111.05788.
- [28] P. Wintz, *Conf. Proc. C* **980420**, 534 (1998).
- [29] W. H. Bertl *et al.* (SINDRUM II), *Eur. Phys. J. C* **47**, 337 (2006).
- [30] T. Suzuki, D. F. Measday, and J. P. Roalsvig, *Phys. Rev. C* **35**, 2212 (1987).
- [31] C. Dohmen *et al.* (SINDRUM II), *Phys. Lett. B* **317**, 631 (1993).
- [32] L. Bartoszek *et al.* (Mu2e), *Mu2e Technical Design Report*, Tech. Rep. (2014) arXiv:1501.05241.
- [33] R. Abramishvili *et al.* (COMET), *Prog. Theor. Exp. Phys.* **2020**, 033C01 (2020), arXiv:1812.09018.
- [34] D. Adhikari *et al.* (PREX), *Phys. Rev. Lett.* **126**, 172502 (2021), arXiv:2102.10767.
- [35] D. Androić *et al.* (Q_{weak}), *Phys. Rev. Lett.* **128**, 132501 (2022), arXiv:2112.15412.
- [36] D. Adhikari *et al.* (CREX), *Phys. Rev. Lett.* **129**, 042501 (2022), arXiv:2205.11593.
- [37] K. Tsukiyama, S. K. Bogner, and A. Schwenk, *Phys. Rev. Lett.* **106**, 222502 (2011), arXiv:1006.3639.
- [38] H. Hergert, S. K. Bogner, T. D. Morris, A. Schwenk, and K. Tsukiyama, *Phys. Rep.* **621**, 165 (2016), arXiv:1512.06956.
- [39] S. R. Stroberg, A. Calci, H. Hergert, J. D. Holt, S. K. Bogner, R. Roth, and A. Schwenk, *Phys. Rev. Lett.* **118**, 032502 (2017), arXiv:1607.03229.
- [40] S. R. Stroberg, S. K. Bogner, H. Hergert, and J. D. Holt, *Ann. Rev. Nucl. Part. Sci.* **69**, 307 (2019), arXiv:1902.06154.
- [41] S. R. Stroberg, J. D. Holt, A. Schwenk, and J. Simonis, *Phys. Rev. Lett.* **126**, 022501 (2021), arXiv:1905.10475.
- [42] K. Hebeler, S. K. Bogner, R. J. Furnstahl, A. Nogga, and A. Schwenk, *Phys. Rev. C* **83**, 031301 (2011), arXiv:1012.3381.
- [43] A. Ekström, B. D. Carlsson, K. A. Wendt, C. Forssén, M. Hjorth-Jensen, R. Machleidt, and S. M. Wild, *J. Phys. G* **42**, 034003 (2015), arXiv:1406.6895.
- [44] W. G. Jiang, A. Ekström, C. Forssén, G. Hagen, G. R. Jansen, and T. Papenbrock, *Phys. Rev. C* **102**, 054301 (2020), arXiv:2006.16774.
- [45] B. S. Hu *et al.*, *Nat. Phys.* **18**, 1196 (2022), arXiv:2112.01125.
- [46] P. Arhuis, K. Hebeler, and A. Schwenk, arXiv:2401.06675.
- [47] G. Hagen *et al.*, *Nat. Phys.* **12**, 186 (2015), arXiv:1509.07169.
- [48] M. Heinz, T. Miyagi, S. R. Stroberg, A. Tichai, K. Hebeler, and A. Schwenk, arXiv:2411.16014.
- [49] T. Miyagi, S. R. Stroberg, P. Navrátil, K. Hebeler, and J. D. Holt, *Phys. Rev. C* **105**, 014302 (2022), arXiv:2104.04688.
- [50] K. Hebeler, V. Durant, J. Hoppe, M. Heinz, A. Schwenk, J. Simonis, and A. Tichai, *Phys. Rev. C* **107**, 024310 (2023), arXiv:2211.16262.
- [51] M. Door *et al.*, arXiv:2403.07792.
- [52] M. Frosini, T. Duguet, J.-P. Ebran, B. Bally, T. Mongelli, T. R. Rodríguez, R. Roth, and V. Somà, *Eur. Phys. J. A* **58**, 63 (2022), arXiv:2111.00797.
- [53] G. Hagen, S. J. Novario, Z. H. Sun, T. Papenbrock, G. R. Jansen, J. G. Lietz, T. Duguet, and A. Tichai, *Phys. Rev. C* **105**, 064311 (2022), arXiv:2201.07298.
- [54] Z. H. Sun, A. Ekström, C. Forssén, G. Hagen, G. R. Jansen, and T. Papenbrock, arXiv:2404.00058.
- [55] D. Gazda, R. Catena, and C. Forssén, *Phys. Rev. D* **95**, 103011 (2017), arXiv:1612.09165.
- [56] C. G. Payne, S. Bacca, G. Hagen, W. G. Jiang, and T. Papenbrock, *Phys. Rev. C* **100**, 061304 (2019), arXiv:1908.09739.
- [57] J. Simonis, S. Bacca, and G. Hagen, *Eur. Phys. J. A* **55**, 241 (2019), arXiv:1905.02055.
- [58] A. Lovato, J. Carlson, S. Gandolfi, N. Rocco, and R. Schiavilla, *Phys. Rev. X* **10**, 031068 (2020), arXiv:2003.07710.
- [59] J. E. Sobczyk, B. Acharya, S. Bacca, and G. Hagen, *Phys. Rev. Lett.* **127**, 072501 (2021), arXiv:2103.06786.
- [60] B. S. Hu, J. Padua-Argüelles, S. Leutheusser, T. Miyagi, S. R. Stroberg, and J. D. Holt, *Phys. Rev. Lett.* **128**, 072502 (2022), arXiv:2109.00193.
- [61] E. Epelbaum, H.-W. Hammer, and U.-G. Meißner, *Rev. Mod. Phys.* **81**, 1773 (2009), arXiv:0811.1338.
- [62] R. Machleidt and D. R. Entem, *Phys. Rep.* **503**, 1 (2011), arXiv:1105.2919.
- [63] H. Hergert, *Front. Phys.* **8**, 379 (2020), arXiv:2008.05061.

- [64] A. L. Fitzpatrick, W. Haxton, E. Katz, N. Lubbers, and Y. Xu, *JCAP* **02**, 004 (2013), arXiv:1203.3542.
- [65] M. Hoferichter, J. Menéndez, and A. Schwenk, *Phys. Rev. D* **102**, 074018 (2020), arXiv:2007.08529.
- [66] G. Hagen, T. Papenbrock, and D. J. Dean, *Phys. Rev. Lett.* **103**, 062503 (2009), arXiv:0905.3167.
- [67] J. E. Sobczyk, B. Acharya, S. Bacca, and G. Hagen, *Phys. Rev. C* **102**, 064312 (2020), arXiv:2009.01761.
- [68] E. Caurier and F. Nowacki, *Acta Phys. Pol.* **30**, 705 (1999).
- [69] E. Caurier, G. Martínez-Pinedo, F. Nowacki, A. Poves, and A. P. Zuker, *Rev. Mod. Phys.* **77**, 427 (2005), arXiv:nucl-th/0402046.
- [70] T. Otsuka, A. Gade, O. Sorlin, T. Suzuki, and Y. Utsuno, *Rev. Mod. Phys.* **92**, 015002 (2020), arXiv:1805.06501.
- [71] A. Poves, J. Sánchez-Solano, E. Caurier, and F. Nowacki, *Nucl. Phys. A* **694**, 157 (2001), arXiv:nucl-th/0012077.
- [72] B. A. Brown and W. A. Richter, *Phys. Rev. C* **74**, 034315 (2006).
- [73] M. Heinz, A. Tichai, J. Hoppe, K. Hebeler, and A. Schwenk, *Phys. Rev. C* **103**, 044318 (2021), arXiv:2102.11172.
- [74] M. Abdullah *et al.*, (2022), arXiv:2203.07361 [hep-ph].
- [75] L. A. Ruso *et al.*, (2022), arXiv:2203.09030 [hep-ph].
- [76] J. Aalbers *et al.*, *J. Phys. G* **50**, 013001 (2023), arXiv:2203.02309 [physics.ins-det].
- [77] J. Aalbers *et al.* (XLZD), (2024), arXiv:2410.17137 [hep-ex].
- [78] M. Hoferichter, J. Ruiz de Elvira, B. Kubis, and U.-G. Meißner, *Phys. Rev. Lett.* **115**, 192301 (2015), arXiv:1507.07552.
- [79] M. Hoferichter, J. Ruiz de Elvira, B. Kubis, and U.-G. Meißner, *Phys. Rep.* **625**, 1 (2016), arXiv:1510.06039.
- [80] D. Siemens, J. Ruiz de Elvira, E. Epelbaum, M. Hoferichter, H. Krebs, B. Kubis, and U.-G. Meißner, *Phys. Lett. B* **770**, 27 (2017), arXiv:1610.08978.
- [81] S. K. Bogner, R. J. Furnstahl, and R. J. Perry, *Phys. Rev. C* **75**, 061001 (2007), nucl-th/0611045.
- [82] K. Levenberg, *Q. Appl. Math.* **2**, 164 (1944).
- [83] D. W. Marquardt, *J. Soc. Indust. Appl. Math.* **11**, 431 (1963).
- [84] M. Newville *et al.*, “lmfit/lmfit-py: 1.3.2,” (2024).
- [85] J. C. Romao and J. P. Silva, *Int. J. Mod. Phys. A* **27**, 1230025 (2012), arXiv:1209.6213.
- [86] M. Hoferichter, P. Klos, J. Menéndez, and A. Schwenk, *Phys. Rev. D* **99**, 055031 (2019), arXiv:1812.05617.
- [87] M. Hoferichter, P. Klos, J. Menéndez, and A. Schwenk, *Phys. Rev. D* **94**, 063505 (2016), arXiv:1605.08043.
- [88] H. de Vries, C. W. de Jager, and C. de Vries, *Atom. Data Nucl. Data Tabl.* **36**, 495 (1987).
- [89] I. Angeli and K. P. Marinova, *Atom. Data Nucl. Data Tabl.* **99**, 69 (2013).